



Effect of Rotation Rate on Microstructure and Mechanical Properties of Friction Stir Processed Ni–Fe-Based Superalloy

Miao Wang^{1,2} · Xing-Wei Huang^{3,4} · Peng Xue³ · Chuan-Yong Cui² · Qing-Chuan Zhang¹

Received: 1 February 2021 / Revised: 8 March 2021 / Accepted: 10 March 2021 / Published online: 2 June 2021
© The Chinese Society for Metals (CSM) and Springer-Verlag GmbH Germany, part of Springer Nature 2021

Abstract

In this work, friction stir processing (FSP) was applied to the high-strength and high-melting-point Ni–Fe-based superalloy (HT700) for the first time with negligible wear of the stir tool. Different rotation rates were chosen to investigate the effect of heat input on microstructure and tensile properties at different temperatures of friction stir processed Ni–Fe-based superalloy. The results showed that with increasing rotation rate, the percentage of high-angle grain boundaries and twin boundaries gradually decreased whereas the grain size initially increased and then remained almost constant; the difference in tensile properties of FSP samples with rotation rates of 500–700 rpm was small attributing to their similar grain size, but the maximum strength was achieved in the FSP sample with a rotation rate of 400 rpm and traverse speed of 50 mm/min due to its finest grain size. More importantly, we found that the yield strength of all FSP samples tensioned at 700 °C was enhanced clearly resulting from the reprecipitation of γ' phase. In addition, the grain refinement mechanism of HT700 alloy during FSP was proved to be continuous dynamic recrystallization and the specific refinement process was given.

Keywords Superalloy · Friction stir processing · Grain refinement · Processing parameter

1 Introduction

To improve the energy efficiency and reduce CO₂ emissions, the steam temperature and pressure have reached the range of 700–760 °C and 35–37.5 MPa in the advanced ultra-supercritical (A-USC) power plants [1–3], respectively. Traditional austenitic and ferritic heat-resistant steels cannot

meet these requirements since their operating temperature is below 650 °C. Thus, Ni-based or Ni–Fe-based superalloys are considered to be the most promising candidates for high temperature components in A-USC programs, such as Inconel 617 [4], Nimonic 263 [5], Inconel 740/740H [2, 6], and GH984 [7]. However, the trade-off between performance and cost has always been a problem for superalloys. Recently, a low-cost Ni–Fe-based superalloy (HT700) with excellent creep properties and better hot workability has been developed as the candidate material for the 700 °C A-USC application [8, 9]. It is primarily strengthened by γ' precipitates and the volume fraction of γ' after aging treatment is about 20% [9]. Its temperature capability is comparable to 740H. More importantly, this Ni–Fe-based superalloy has a much lower cost and better hot workability compared to 740H [8].

Friction stir processing (FSP) is a simple solid-state metal-working technique derived from friction stir welding (FSW) [10, 11]. FSW/FSP has a simple basic concept. The rotating tool with pin and shoulder is inserted into the workpiece at high speed and then traverses in a direction of interest. The heating is mainly obtained by friction between the tool and workpieces [12]. Local heating softens the material and permits a considerable amount of plasticity around the pin,

Available online at <http://link.springer.com/journal/40195>.

✉ Chuan-Yong Cui
chycui@imr.ac.cn

✉ Qing-Chuan Zhang
zhangqc@ustc.edu.cn

¹ CAS Key Laboratory of Mechanical Behavior and Design of Materials, University of Science and Technology of China, Hefei 230027, China

² Superalloy Division, Institute of Metal Research, Chinese Academy of Sciences, Shenyang 110016, China

³ Shenyang National Laboratory for Materials Science, Institute of Metal Research, Chinese Academy of Sciences, Shenyang 110016, China

⁴ School of Materials Science and Engineering, University of Science and Technology of China, Hefei 230027, China

resulting in refinement and modification of the microstructure in the stir zone (SZ). FSP has been successfully employed to fabricate surface composite, modify microstructures, enhance mechanical properties, and synthesize composite compounds [11]. Therefore, FSP has attracted much attention in a relatively short time since its development.

FSW/FSP has been certified to be a promising technique originally developed for light weight materials, such as aluminum and magnesium alloys [13]. However, its application in high-melting-point materials is restricted due to the wear of the tool. Unfortunately, in this context, researches mainly focus on the FSW/FSP of titanium, high-entropy alloys, stainless steels, etc. [14–17]. Superalloys usually have a higher strength and harder plastic flow than other high-melting-point materials at elevated temperatures making it more challenging to apply FSP/FSW to them, so that only a few studies have been reported in this field [18, 19]. To solve this problem, heat-assisted FSW/FSP has been proposed to improve the rheological properties of the material [20, 21]. However, the complex operation and introduced new parameters set strict limits on its application. In conclusion, applying FSP to superalloys is very difficult and few attempts have been made to it. To the best of the authors' knowledge, no research on the application of FSP in Ni–Fe-based superalloy (HT700) has been reported thus far. Whether high-strength Ni–Fe-based superalloy can be subjected to FSP without tool wear remains unclear and the microstructure and mechanical properties of the friction stir processed (FSPed) HT700 alloy are not well understood. Thus, research on the FSP of a new Ni–Fe-based superalloy is quite necessary.

The microstructure and the resulting mechanical properties of FSP/FSW samples are significantly affected by the material flow behavior and thermal cycle, both of which depend on the processing parameters, including rotation rate, traverse speed, tool tilt angle, tool geometry, cooling rate, etc. [22]. The rotation rate and traverse speed are the major parameters among them. So far, limited researches have been done on the effect of processing/welding parameters on microstructure and mechanical properties of friction stir processed/welded superalloys. In particular, only the effect of traverse speed has been investigated. Song et al. [18] studied the effect of welding speed on microstructural and mechanical properties of friction stir welded (FSWed) Inconel 600. The results suggested that with increasing welding speed, the grain size, as well as the fraction of high-angle grain boundaries (HAGBs) and twin boundaries (TBs) decreased, while the microhardness and the ultimate tensile strength (UTS) of FSW samples increased. Ahmed et al. [23] reported that by the increase of the welding

speed, the hardness of the FSWed Ni-based superalloy Inconel 718 significantly increased due to the reduction of the grain size. Nevertheless, extremely little attention has been paid to the effect of the rotation rate. It is worth emphasizing that the rotation rate plays a significant role in the microstructure evolution because it determines the thermal power during FSP/FSW at constant downward force and tool geometry. Therefore, the effect of rotation rate on microstructure and mechanical properties of FSPed superalloys needs further investigation.

This study aims to investigate the effect of the rotation rate on microstructure and mechanical properties of FSP samples, compare the strength and fracture mechanism of the base material (BM) and FSP samples at different temperatures, and analyze the grain refinement mechanism of HT700 alloy during FSP. These preliminary studies are expected to play a significant role in promoting the application and development of FSP of HT700 alloy.

2 Experimental

A 4-mm-thick plate of HT700 alloy was used in this study. Its chemical composition is listed in Table 1. The alloy was melted in a vacuum induction furnace and homogenized at 1200 °C for 24 h, followed by forging at 1150 °C. The sample was solution-treated at 1100 °C for 1 h, and then water quenching. The microstructure of the alloy after solution treatment is taken as the initial structure (the microstructure of the BM) for FSP, as shown in Fig. 1. The coarse equiaxed grains (~77 μm) and a few annealing twins were observed in the BM. In addition, the carbide particles were detected inside the grains and on the grain boundaries (GBs). The

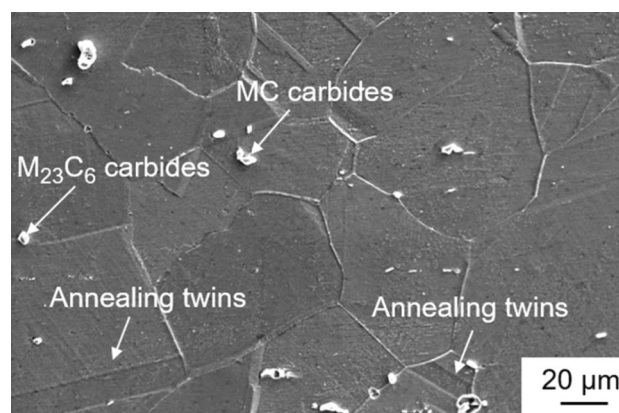


Fig. 1 Microstructure of the base material

Table 1 Chemical composition of HT700 alloy (wt%)

Fe	Cr	Al	Ti	Cu	W + Mo + Nb	Si + Mn + C + B	Ni
20	18	1.8	2.4	0.15	2.8	0.715	Bal

carbides presented inside the grains were suggested to be MC-type carbide, and M was mostly substituted for Ti and Nb [24]. The carbides formed on the GBs were $M_{23}C_6$ -type carbide, and M was mostly substituted for Cr and Fe [24].

The tool used in the FSP was fabricated from tungsten–rhenium (W–Re) with a shoulder diameter of 11 mm and a conical pin of 6 mm in root diameter, 3.65 mm in tip diameter, and 1.6 mm in length (Fig. 2). FSP was carried out with a traverse speed of 50 mm/min and rotation rates of 400–700 rpm, respectively. The detailed FSP parameters are indicated in Table 2. The tool tilt angle was 3° and the plunge depth was 0.3 mm. During FSP, argon shielding was employed to prevent surface oxidation.

Dog-bone-shaped tensile samples with a gauge length of 2.5 mm, a width of 1.4 mm, and a thickness of 0.55 mm were cut from the center of the SZ (Fig. 2). The BM was selected for the comparison experiment. Uniaxial tensile tests were performed on an Instron 5458 tester at room temperature (RT), 400 °C, and 700 °C using a strain rate of $3 \times 10^{-4} \text{ s}^{-1}$. When samples tensioned at 400 °C and 700 °C, tensile samples were put into the tester at the set temperature and kept at this temperature for 5 min before tensile tests.

Optical microscope (OM) was used to observe the nonuniform grain size in the SZ. The fracture surfaces were characterized by scanning electron microscope (SEM). The detailed microstructure features in the SZ were analyzed using electron backscatter diffraction (EBSD) and scanning transmission electron microscope (STEM). Samples for OM and SEM studies were etched with 100 ml HCl + 100 ml CH_3OH + 50 g CuCl_2 solution. For the EBSD studies, mechanical polishing and ion etching were performed to eliminate the surface stress layer. EBSD scans were performed with a step size of 0.3 μm at 20 kV. Limited by the accuracy of EBSD, only grain-boundary misorientation angles greater than 2° were considered. For STEM observation, thin foils were cut from the FSP sample

Table 2 Detailed FSP parameters

Sample	Rotation rate (rpm)	Traverse speed (mm/min)
400/50	400	50
500/50	500	50
600/50	600	50
700/50	700	50

along the transverse direction and prepared by twin jet polishing in a solution of 10% perchloric acid and 90% ethanol at $\sim 50 \text{ mA}$ and -30°C .

3 Results and Discussion

3.1 Low Magnification Overview

Figure 3 shows the transverse cross section macrostructure of FSP samples with different rotation rates. They all exhibited a basin-shaped structure widening toward the upper regions [25]. Moreover, it can be observed that the depth of the widening zone became high with increasing rotation rate (shown by the red lines), which indicated that with the increase of the rotation rate, the influence of the shoulder became strong.

During FSP, the relationship of the temperature (T) and processing parameters in the SZ can be expressed as [26–28]:

$$\frac{T}{T_m} = K \left(\frac{\omega^2}{v \cdot 10^4} \right)^\alpha, \quad (1)$$

where T_m is the alloy melting point, ω is the rotation rate, v is the traverse speed, K and α are constants, varying between 0.65–0.75 and 0.04–0.06, respectively.

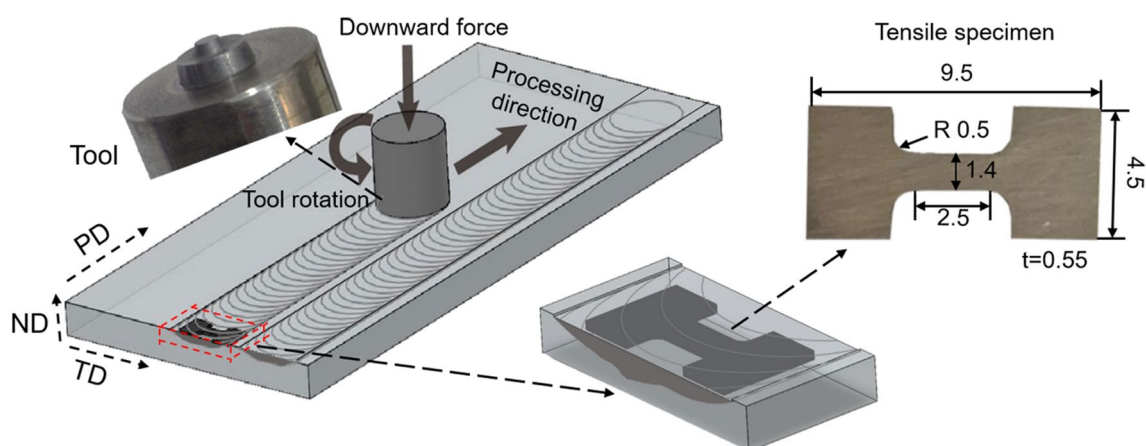


Fig. 2 Schematic of FSP and geometry of extracted tensile and tool; PD, ND, and TD correspond to processing, normal, and transversal directions, respectively

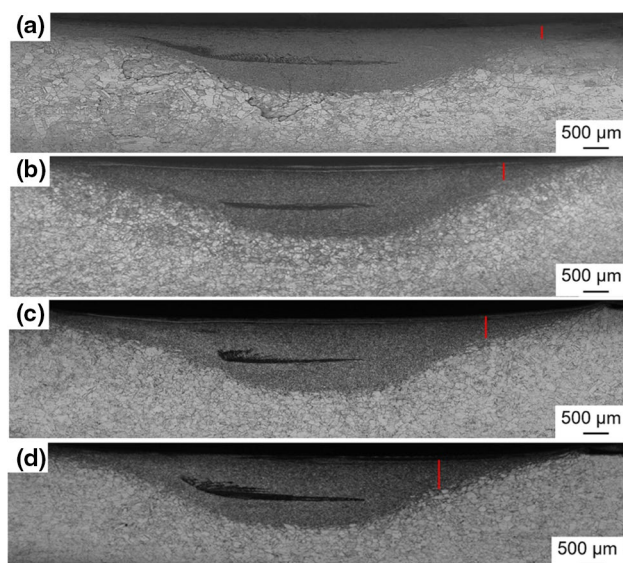


Fig. 3 Low magnification overview of the transversal cross section of different FSP samples: **a** 400/50, **b** 500/50, **c** 600/50, **d** 700/50. Red lines correspond to the influence of the shoulder

Because superalloys have significant resistance to metallic plastic deformation, the actual plunge depth was less than 0.3 mm. According to Eq. (1), the heat input during FSP increases with increasing rotation rate, resulting in the decrease in the significant resistance to metallic plastic deformation. Therefore, with the increase of the rotation rate, the actual plunge depth increased, making a stronger action of the shoulder.

The structure of 600/50 was investigated in detail, as shown in Fig. 4. Four typical zones can be identified in the transverse cross section macrostructure: the SZ, thermomechanical-affected zone (TMAZ), heat-affected zone (HAZ), and BM (Fig. 4a). The fine equiaxed grains were obtained in the SZ owing to the action of strong plastic deformation and dynamic recrystallization (DRX) [29, 30]. The TMAZ was next to the SZ, and the grains in this area experienced shear deformation and practical DRX [31, 32], as shown in subfigure 1 of Fig. 4a. The microstructure in the HAZ was determined by heat input during FSP, and a large number of TBs were observed in this area, as shown in subfigure 2 of Fig. 4a. The BM was close to the HAZ, and it underwent neither strain nor thermal energy from processing. After FSP, the length of the pin was still about 1.6 mm, which was the same as before, indicating that the tool was hardly worn. In addition, the actual penetration-depth (1.7 mm) was smaller than the theoretical penetration-depth (1.9 mm), which also indicated that the actual plunge depth was less than 0.3 mm.

Two sides of the SZ with a characteristic asymmetry were created due to the translation of the rotating tool, including the advancing side (AS) and retreating side (RS). Different locations in the SZ have various temperatures. Moreover,

numerous studies have proved that the microstructure of fine grains in the SZ was nonuniform [33–35]. Thus, the four positions in the SZ were measured, as shown in Fig. 4b–e. They were taken at the AS, RS, top, and bottom, respectively, corresponding to positions b–e in Fig. 4a. No significant difference in grain size between AS (Fig. 4b) and RS (Fig. 4c) was found. However, the grain size at the top (Fig. 4d) was smaller than that at the bottom (Fig. 4e) due to its higher cooling rate. Moreover, it has been indicated that the average grain size in the central zone of the SZ was almost identical to that in the entire SZ [35], and the uniform microstructure in the SZ has usually assumed to discuss the mechanical properties of the FSP sample. Therefore, the microstructure in the center zone of the SZ (shown by the red rectangle in Fig. 4a) was selected for investigation.

3.2 Effects of Rotation Rate on Microstructure

The heat input and cooling rate are the main factors affecting the microstructure in the SZ. Therefore, it is necessary to select different rotation rates to investigate the effect of heat input on microstructure and mechanical properties in the SZ. Here, the effect of rotation rate on microstructure was analyzed using EBSD. Figure 5a–d shows the EBSD orientation micrographs of 400/50, 500/50, 600/50, and 700/50, respectively. Different colors in the grain orientation micrograph represent different crystallographic orientations. The corresponding statistical distributions of grain size are shown in Fig. 5e–h, and they all conformed to the Gaussian distribution function (shown by the black curve). The grain sizes were significantly refined from 77 μm in the BM to 4–6 μm in the SZ due to the action of DRX. Moreover, it can be observed that the grains of the 400/50 were the finest and most homogeneous. Figure 6 shows the variation of grain size in the SZ with increasing rotation rate. As the rotation rate increases from 400 to 600 rpm, the grain size gradually increased, with 4.37 μm at 400 rpm, 5.72 μm at 500 rpm, and 6.01 μm at 600 rpm. With the further increase of the rotation rate, the average grain size reduced from 6.01 μm in the 600/50 to 5.73 μm in the 700/50, but the reduction was not obvious. With the change of the rotation rate, the grain size was maintained in the range of about 4–6 μm .

During FSP, fine equiaxed grains can be obtained in the SZ by DRX resulting from high heat input and severe plastic deformation [35]. DRX grains in the SZ also undergo static grain growth during the cooling of the thermal cycle and this process benefit from increasing temperature [36]. A higher rotation rate results in more heat input (Eq. (1)). Hence, the grain size gradually increased with increasing rotation rate from 400 to 600 rpm. It has been proved that increasing strain rate or lowering heat input contribute to grain refinement [37]. Increasing rotation rate not only introduces high heat input to promote the growth of recrystallized

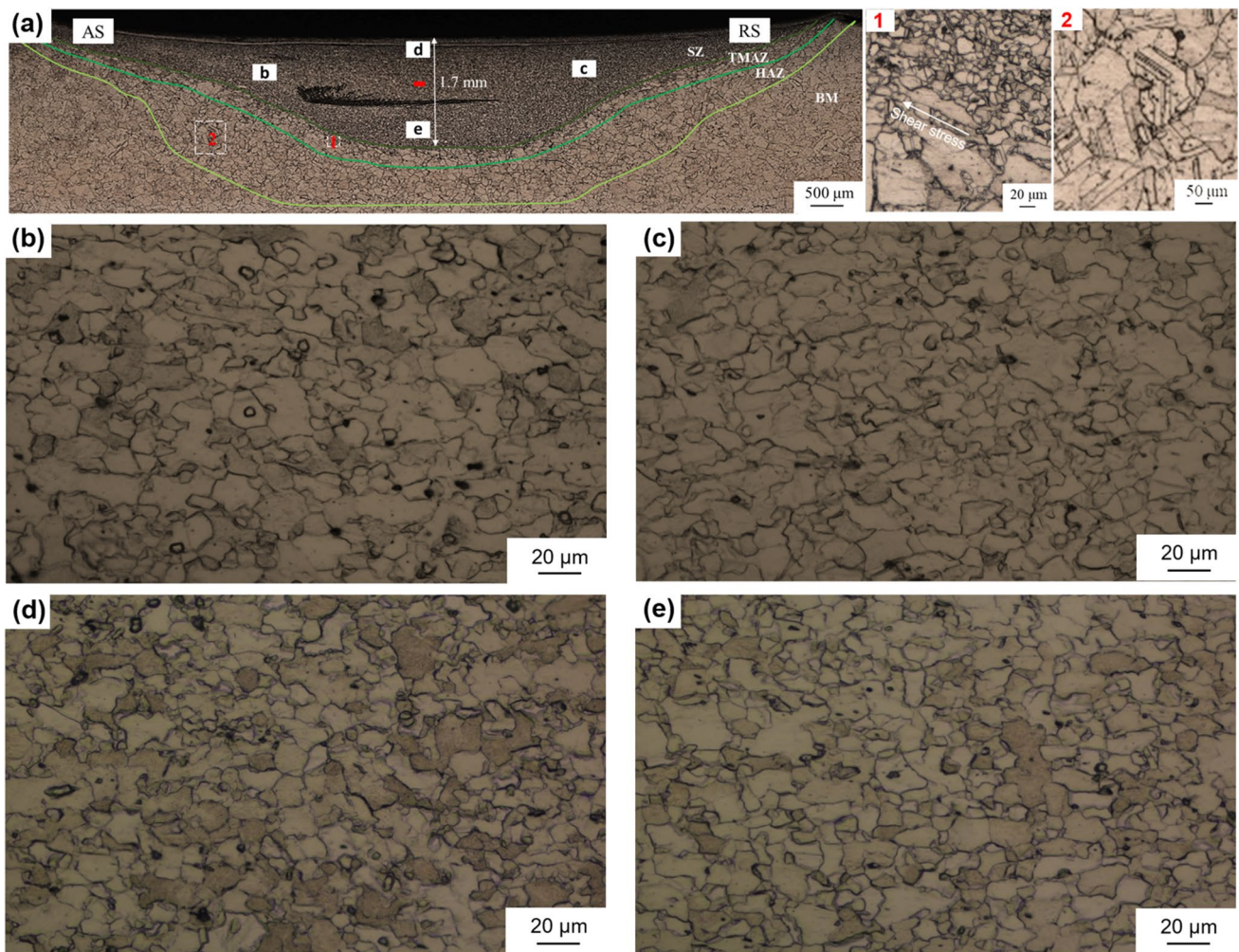


Fig. 4 **a** Low magnification overview of the transversal cross section of the FSP sample 600/50, subfigures 1 and 2 are enlarged images of the part marked by the dotted rectangle. **b–e** OM micrographs taken at various locations in the SZ corresponding to the location shown in **a**. AS is the advancing side, where the direction of the tool rotation is the same as that of the tool translation, and RS is the retreating side, where they are opposite

grains, but also brings about a large strain rate to refine the grains. Moreover, according to Eq. (1), the rate of temperature increase becomes slow with increasing rotation rate, and the similar result has been reported by Sato et al. [38], i.e., when the rotation rate beyond 2000 rpm, the rate of temperature increase of Al alloy 6063 became very slow with further increasing rotation rate. Therefore, the promotion effect of high heat input on the growth of recrystallized grains becomes weak whereas the action of a large strain rate becomes strong at 700 rpm. Hence, when the rotation rate was increased from 600 to 700 rpm, there was no obvious change in the grain size with only a little reduction (Fig. 6). Finally, the grain size of FSP samples was maintained at values of 4–6 μm .

Figure 7a–d shows the EBSD micrographs of grain boundaries characteristics of 400/50, 500/50, 600/50, and 700/50, respectively. The high-angle grain boundaries

(HAGBs, $\geq 15^\circ$) and low-angle grain boundaries (LAGBs, 2° – 15°) are marked with black and green lines, respectively. The grain-boundary misorientation angle distribution of FSP samples with different rotation rates is shown in Fig. 7e–h, and the red curve is grain misorientation random distribution of the face-centered-cubic (FCC) crystallization structure. It can be observed that the fractions of the misorientation angles in 2° – 5° of all FSP samples were above 20%, and it increased with increasing rotation rate. The formation of these LAGBs was attributed to the dynamic recovery (dislocation accumulation and rearrangement) [39]. In addition, the percentage of HAGBs (HAGBs%) was calculated. The results showed that HAGBs% was 65.1% at 400 rpm, 63.4% at 500 rpm, 60.3% at 600 rpm, and 58.1% at 700 rpm, respectively. With the increase of the rotation rate, the HAGBs% gradually decreased, which was consistent with the increase of

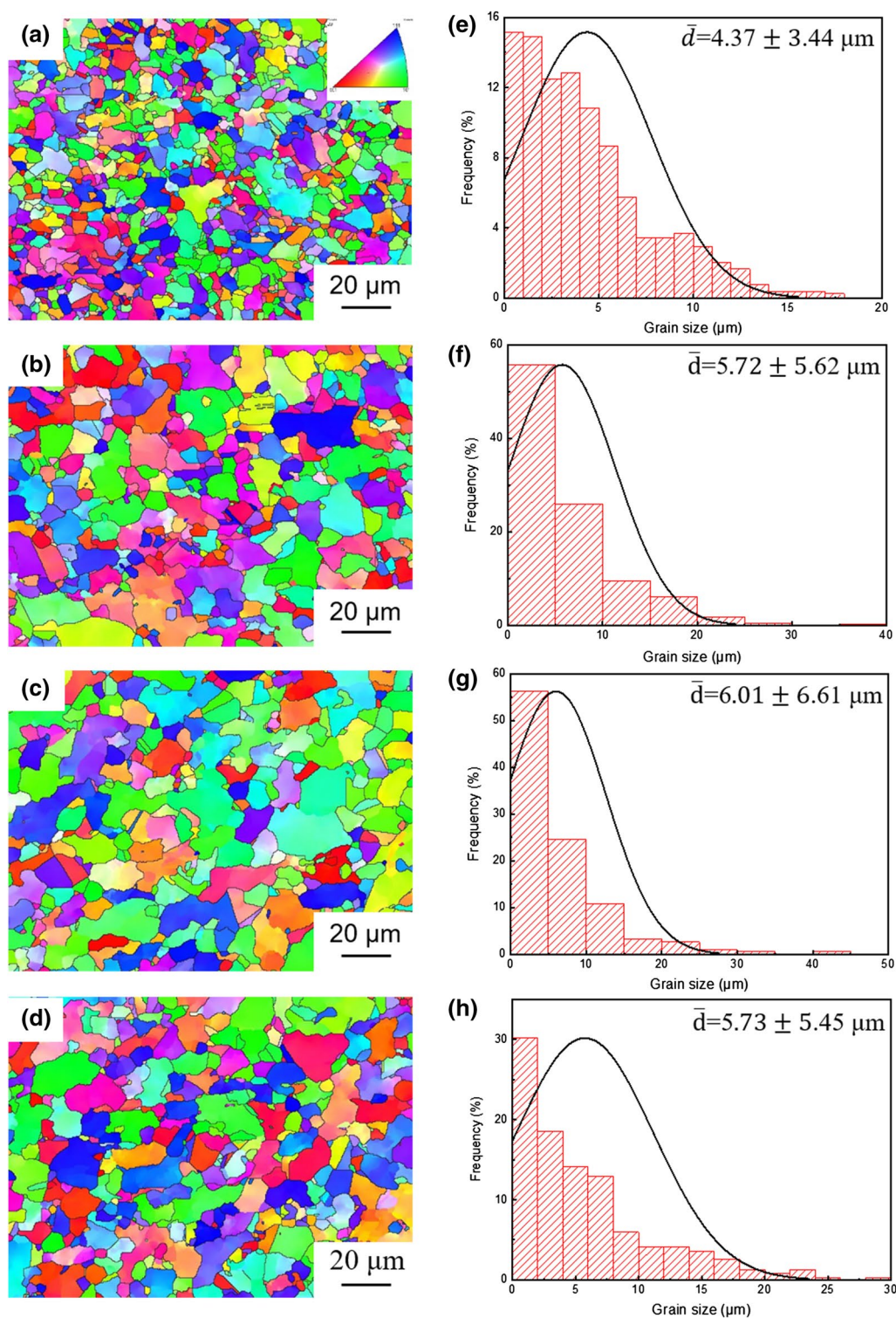


Fig. 5 EBSD orientation maps of crystallized grains and corresponding grain size distribution of different FSP samples: **a** and **e** 400/50, **b** and **f** 500/50, **c** and **g** 600/50, **d** and **h** 700/50

misorientation angles in 2° – 5° . During FSP, the heat input increases with increasing rotation rate (Eq. (1)). Therefore, it will take more time to drop the temperature in the SZ below the dynamic recovery temperature at a higher

rotation rate. In other words, the action of the dynamic recovery will last longer at a higher rotation rate. Therefore, with the increase of the rotation rate, more LAGBs will be formed, resulting in the reduction of the HAGBs%.

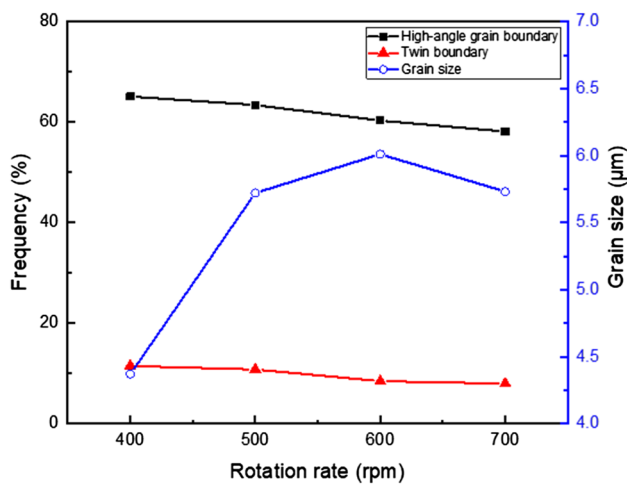


Fig. 6 Variation of grain size and misorientation fraction in the SZ with increasing rotation rate

As shown in Fig. 7e–h, the misorientation angle of 60° was a large peak in FSP samples. It has been identified as the sigma three ($\Sigma 3$) TBs in the FCC materials [10], which were shown by the red lines in Fig. 8. The percentage of TBs (TBs%) was 11.5%, 10.8%, 8.47%, and 7.99% at the rotation rate of 400 rpm, 500 rpm, 600 rpm, and 700 rpm, respectively. Figure 6 shows the variation of TBs% with increasing rotation rate. It can be concluded that by the increase of the rotation rate, the TBs% gradually decreased. According to Eq. (1), a higher rotation rate usually leads to higher heat input. Moreover, it is worth noting that the critical resolved shear stress (CRSS) for twinning is hardly affected by temperatures, while the CRSS for dislocation slip significantly decreases with increasing temperature. The high temperature promotes the dislocation slip, thereby limiting the twinning to some extent. Thus, the TBs% decreased with increasing rotation rate.

3.3 Mechanism of Grain Refinement

The grain structure in the SZ is controlled by DRX which is caused by high heat input and severe plastic deformation during FSP/FSW [20, 37]. The DRX can significantly refine the grain size and reduce the deformation resistance, which is beneficial to improve the mechanical properties of the metals [40]. The studies of the microstructure evolution and grain refinement of materials during FSP/FSW usually focus on the DRX. The present study is the first reported research on the FSP of HT700 alloy. Therefore, it is extremely necessary to investigate the grain refinement mechanism of HT700 alloy during FSP. The continuous dynamic recrystallization (CDRX) and discontinuous dynamic recrystallization (DDRX) are the two main types of DRX in Ni-based superalloy. DDRX includes two steps:

the nucleation of new grains and grain growth, and this mechanism is featured by bulging of the grain boundaries. CDRX is a strong recovery process, i.e., the HAGBs and new grains are formed by continuously absorbing dislocations into subgrain boundaries. Jazaeri et al. [41] pointed out that HAGB% initially decreases and then increases until saturating in the range of 60–80% with increasing strain, during deformation. Besides, it has been indicated that the change of HAGB% during annealing can provide a reliable method of identifying the DRX process [42, 43]. A sharp increment of the HAGB% means the occurrence of DDRX; however, when CDRX occurs, HAGB% remains almost constant. During FSP, materials experience severe plastic deformation and high temperature, which is similar to the process including severe plastic deformation (SPD) and the subsequent annealing [10]. Moreover, the HAGB% was at values of 58.1–65.1% at present work, which corresponded to the range of HAGB% obtained by deformation. This implies that the HAGB% remains almost constant during annealing. Therefore, it can be concluded that CDRX should be the major nucleation mechanism of DRX for HT700 alloy during FSP. To further prove the occurrence of CDRX, the STEM results of 500/50 were studied, as shown in Fig. 9. Dislocations and dislocation structures (e.g., dislocation tangle zones (DTZs), dislocation cells (DCs), dislocation walls (DWs), etc.) were very easily detected inside recrystallized grains. In general, when CDRX occurs, recrystallized grains still have dislocations. On the contrary, recrystallized grains are nearly free of dislocation with the action of DDRX [44]. Hence, the grain refinement mechanism of HT700 alloy during FSP is CDRX.

Based on the above conclusion, the specific grain refinement process is explained as follows. First, the dislocation pile-up near the initial grain boundaries and inside the deformed grains forming DTZs. Second, when dislocation density is high enough, the dislocations rearrangement and annihilation occur to reduce the stored energy, and DCs are formed. Third, DCs transform into subgrains resulting from the lattice rotation of DCs. Finally, LAGBs evolve into HAGBs by increasing the progressive misorientation and new recrystallized grains are generated.

3.4 Effects of Rotation Rate on Mechanical Properties

Figure 10 shows the engineering stress–strain curves of the BM and FSP samples tensioned at RT, 400 °C, and 700 °C, respectively. Meanwhile, important mechanical characterization yield strength (YS), ultimate tensile strength (UTS), and elongation obtained during tensile tests at different temperatures are presented in Fig. 11. At RT, the FSP samples showed a slightly higher YS than the BM, but the UTS of the former was lower than that of the latter (Fig. 10a).

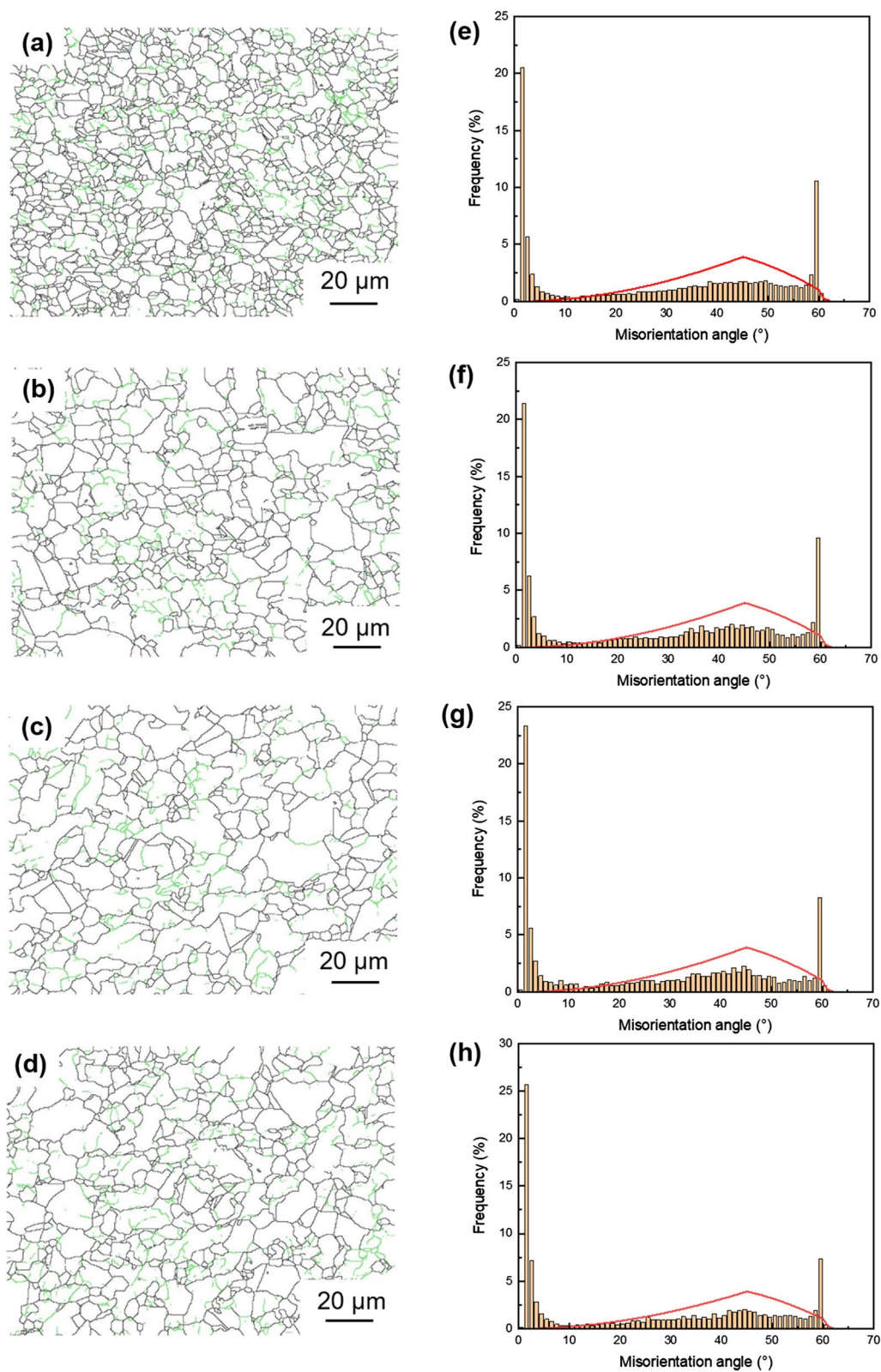


Fig. 7 EBSD maps showing grain boundaries characteristics and the corresponding distribution of grain-boundary misorientation angle of different FSP samples: **a** and **e** 400/50, **b** and **f** 500/50, **c** and **g** 600/50, **d** and **h** 700/50

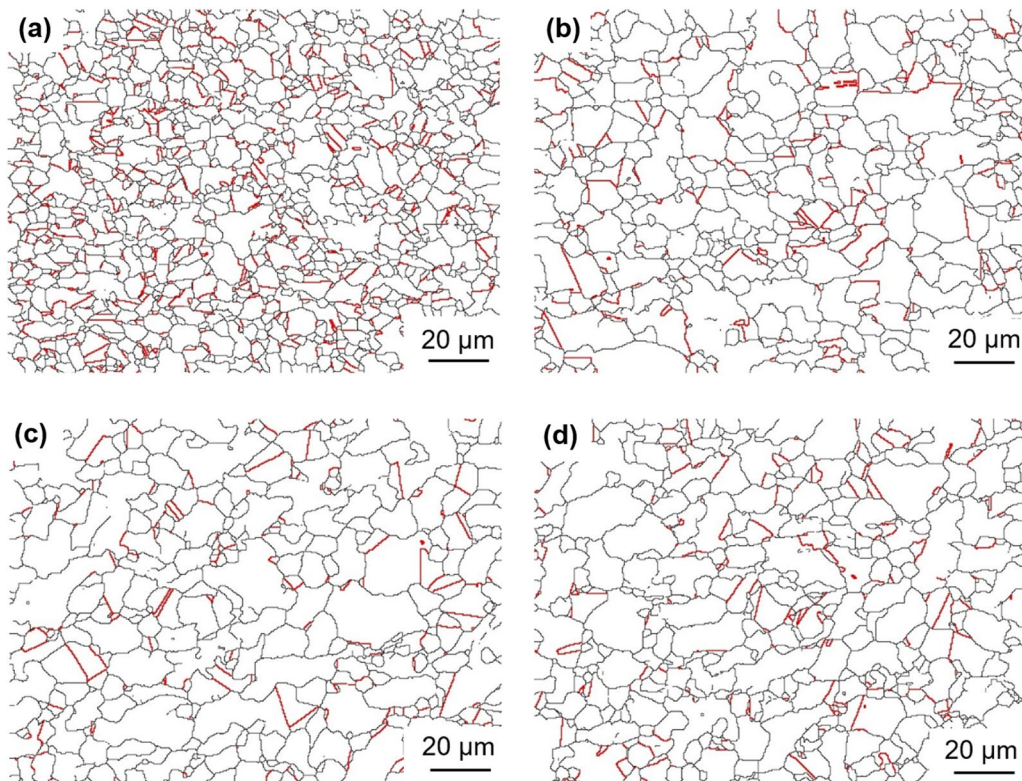


Fig. 8 EBSD maps showing the arrangement of sigma three ($\Sigma 3$) twin boundaries in different FSP samples: **a** 400/50, **b** 500/50, **c** 600/50, **d** 700/50

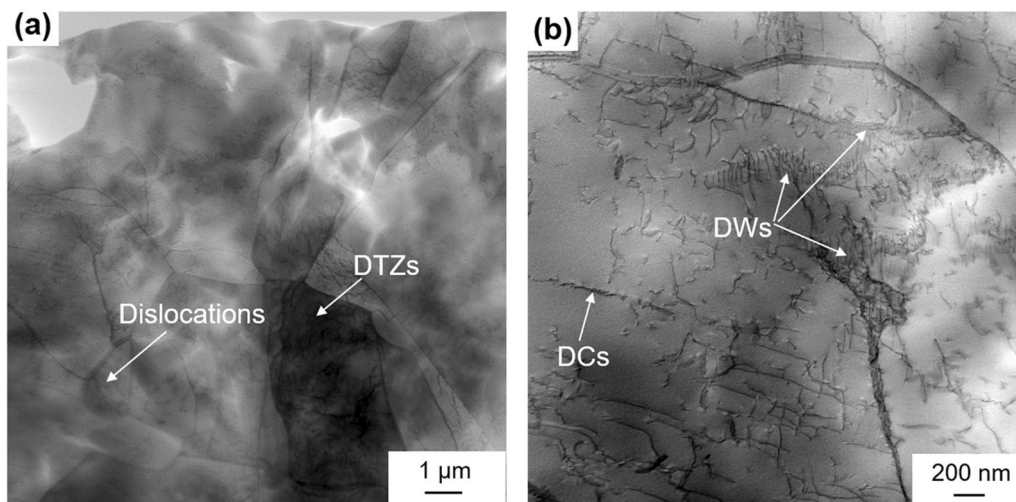


Fig. 9 STEM micrographs showing dislocations and dislocation structures of 500/50 FSP sample: **a** structure of dislocations and dislocation tangle zones at low magnification, **b** structure of dislocation cells and dislocation walls at higher magnification (DTZs, DCs, and DWs correspond to dislocation tangle zones, dislocation cells, and dislocation walls, respectively)

At 400 °C, the YS of the FSP samples was slightly higher than that of the BM, but their UTS was similar (Fig. 10b). Moreover, Portevin–Le Chatelier (PLC) effect or serrated flow was found at this temperature, which is attributed to the interaction between mobile dislocations and solution

atoms [45–48]. At 700 °C, both YS and UTS increased clearly after FSP (Fig. 10c). For ductility, BM and FSP samples all exhibited an excellent elongation at RT and 400 °C. However, all samples had a very low elongation (< 10%) at 700 °C. Thus, the mechanical properties of

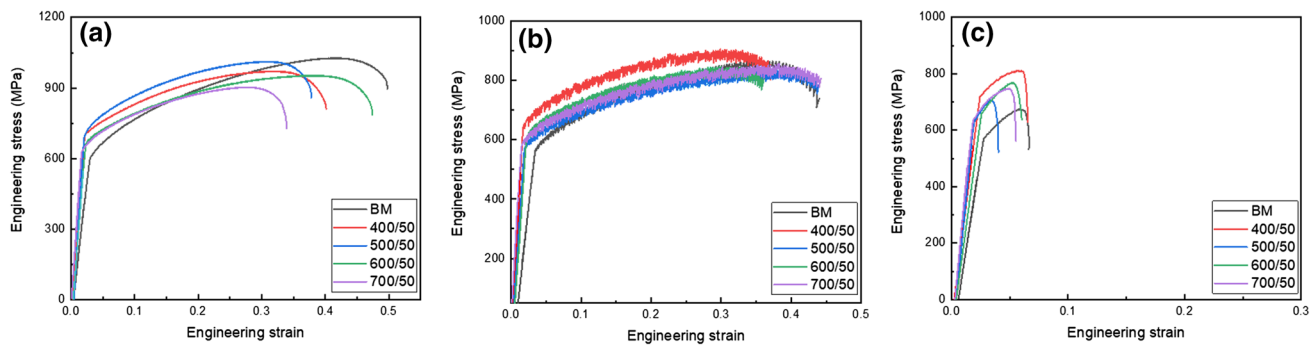


Fig. 10 Engineering stress–strain curves of the BM and FSP samples at different temperatures: **a** RT, **b** 400 °C, **c** 700 °C

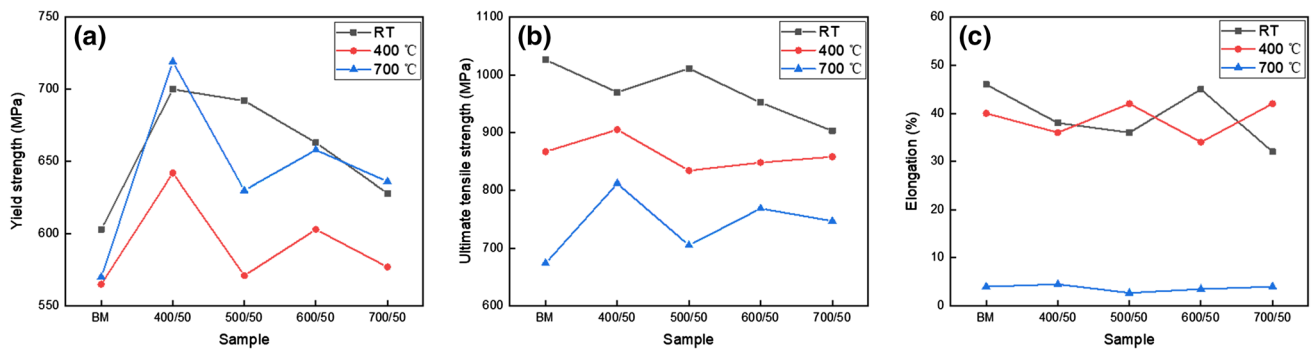


Fig. 11 Mechanical properties of the BM and FSP samples tensioned at different temperatures: **a** yield strength, **b** ultimate tensile strength, **c** elongation.

HT700 alloy were improved through FSP. In addition, it can be indicated that the maximum strength was achieved in 400/50 but the rotation rate had little influence on tensile properties of FSP samples with rotation rates of 500–700 rpm at all temperatures (Fig. 11a, b). Moreover, the elongation of FSP samples with different rotation rates was similar (Fig. 11c). Therefore, it can be demonstrated that the optimal parameters were the rotation rate of 400 rpm and the traverse speed of 50 mm/min.

The strengthening methods of the superalloys mainly include precipitation strengthening, grain-boundary strengthening, and solid-solution strengthening. For precipitation-hardened superalloys, the solid-solution strengthening can be ruled out due to their indistinctive strengthening. The grain-boundary strengthening of polycrystalline alloys has been suggested by the Hall–Petch relationship which is used to express the relationship between the YS and the average grain size of the metals [49]:

$$\sigma_y = \sigma_0 + Kd^{-\frac{1}{2}}, \quad (2)$$

where σ_y is the YS, σ_0 is the resistance to deformation in the crystal, K ($750 \text{ MPa } \mu\text{m}^{1/2}$ [50]) is a constant in the same material, and d is the diameter of grains. Here, σ_0 can be

omitted because only the grain-boundary strengthening was considered [50]:

$$\sigma_y = Kd^{-\frac{1}{2}}. \quad (3)$$

According to the Hall–Petch relationship, the YS of metals increases with decreasing the average grain size. For the BM, $\sigma_y = 750 \times 77^{-\frac{1}{2}} \approx 85$ (MPa); For the 400/50, $\sigma_y = 750 \times 4.37^{-\frac{1}{2}} \approx 359$ (MPa). A remarkable improvement in the strength of FSP samples is attributed to their significant refined grain size.

Precipitation strengthening is also a major strengthening mechanism of HT700 alloy. It has been proved that precipitation strengthening depends on the size and volume fraction of precipitation [51]. The high volume fraction of the γ' precipitates will enhance the precipitation strengthening of superalloys [52]. The influence of the γ' size on precipitation strengthening is determined by the dislocation–precipitation interaction mechanism. It has been proved that the dominant strengthening mechanism in the friction welded joint of HT700 alloy is the weakly coupled dislocation (WCD) shearing mechanism [53]. The microstructure between the friction welded joint and SZ is similar, so it can be inferred that the dominant strengthening mechanism of FSP samples

is WCD shearing mechanism, which can be expressed as [53]:

$$\Delta\sigma_{\text{WCD}} \approx M\Delta\tau_c = \frac{M\gamma_{\text{APB}}}{2b} \left[\left(\frac{6\gamma_{\text{APB}}fr}{\pi T} \right)^{\frac{1}{2}} - f \right], \quad (4)$$

where $\Delta\sigma_{\text{WCD}}$ is the stresses contributed from WCD shearing mechanism, τ_c is the critical resolved shear stress, M is the Taylor factor, b is the Burgers vector of $\frac{a}{2}\langle 110 \rangle$, γ_{APB} is the APB energy, T is the line tension of the dislocations, f and r are the volume fraction and the radius of the γ' precipitates, respectively. According to Eq. (4), the $\Delta\sigma_{\text{WCD}}$ decreases with decreasing r . To sum up, the precipitation strengthening of FSP samples decreases with decreasing the size and volume fraction of precipitation.

The γ' precipitates in the BM are completely dissolved during the heating cycle of FSP because the temperature in the SZ exceeds the dissolution temperature of γ' precipitates [53, 54]. Then, only a fraction of fine γ' reprecipitated during the rapid cooling, which is called reprecipitated γ' [20, 53]. Xu et al. [53] reported that the diameter and volume fraction of reprecipitated γ' in the friction welded joint of HT700 alloy were only 6.7 ± 0.9 nm and 8.9%, respectively, both of which were much smaller than those of the BM (35 ± 8 nm and 20%). Therefore, it can be inferred that the size and volume fraction of the γ' in the SZ both were much lower than that of the BM, and similar results have been reported in Refs. [20, 53, 54]. Therefore, the contribution of precipitation strengthening of FSP samples was significantly lower than that of the BM. As the results of the integrated influence of the grain-boundary and precipitation strengthening, the YS of FSP samples was slightly higher than that of the BM at RT and 400 °C. More importantly, post-process heat treatment can improve the mechanical properties of the precipitation-hardened FSP samples by increasing the amount of precipitation [55]. The amount of reprecipitated γ' in FSP samples was very low leaving adequate γ' forming elements Al and Ti in the γ matrix. The sufficient driving force for the formation of γ' may contribute to the reprecipitation of γ' during tensile tests at 700 °C, leading to a greater contribution of precipitation strengthening of FSP samples [56]. Therefore, high strength was achieved in FSP samples tensioned at 700 °C. Moreover, due to the reprecipitation of γ' during tensile tests at 700 °C, the YS of all FSP samples tensioned at 700 °C was higher than that at 400 °C. In addition, the UTS of the FSP samples tensioned at 700 °C were significantly lower than that at RT and 400 °C because of their poor ductility and weak work-hardening ability.

For FSP samples, the strength is strongly affected by its average grain size because grain-boundary strengthening is

the most effective method for strengthening. The difference in grain size between FSP samples with rotation rates of 500–700 rpm was small, resulting in their similar strength. Therefore, the rotation rates had little influence on tensile properties of them. Nevertheless, the 400/50 had the highest strength due to its finest grain size. Hence, on the premise of no defects producing, reducing the heat input also will conducive to improving the mechanical properties of FSPed HT700 alloy.

3.5 Fracture Mechanism

It can be inferred that FSP samples have the same deformation mechanism because they exhibited similar stress–strain curve shapes at all temperatures (Fig. 10). Thus, the fracture surfaces of 400/50 and 500/50 were chosen to investigate the fracture behavior of FSP samples during tensile tests. The SEM micrographs of the fracture surface of the BM and FSP samples tensioned at RT, 400 °C, and 700 °C are shown in Figs. 12 and 13, respectively. The fracture surfaces of the BM and FSP samples tested at RT and 400 °C showed similar features of typical dimples and shear lips (Figs. 12a–d and 13a–d, g–j), indicating that the BM and FSP samples tensioned at RT and 400 °C have relatively high ductility [57]. Due to the FSP samples displayed smaller, shallower, but more quantity and uniform dimples than the BM, their ductility were comparable to the BM. Figure 12e and f shows the fracture surfaces of the BM tested at 700 °C. The fracture surface was characterized by a mixture of intergranular and transgranular fractures, and the intergranular fracture was the dominant fracture mode. Meanwhile, the secondary cracks were observed [58]. The fracture surfaces of FSP samples tensioned at 700 °C are shown in Fig. 13e, f, k, and l. The typical intergranular fracture was observed over the whole fracture surface. The intergranular fracture is a characteristic of brittle behavior. Therefore, the BM and FSP samples had a bad ductility, which was corresponding well with the tensile curves (Fig. 10c).

4 Conclusions

In this work, the effect of rotation rate on microstructure evolution and mechanical properties of FSPed HT700 alloy, as well as the grain refinement mechanism of HT700 alloy during FSP was studied. The main conclusions of this work are as follows:

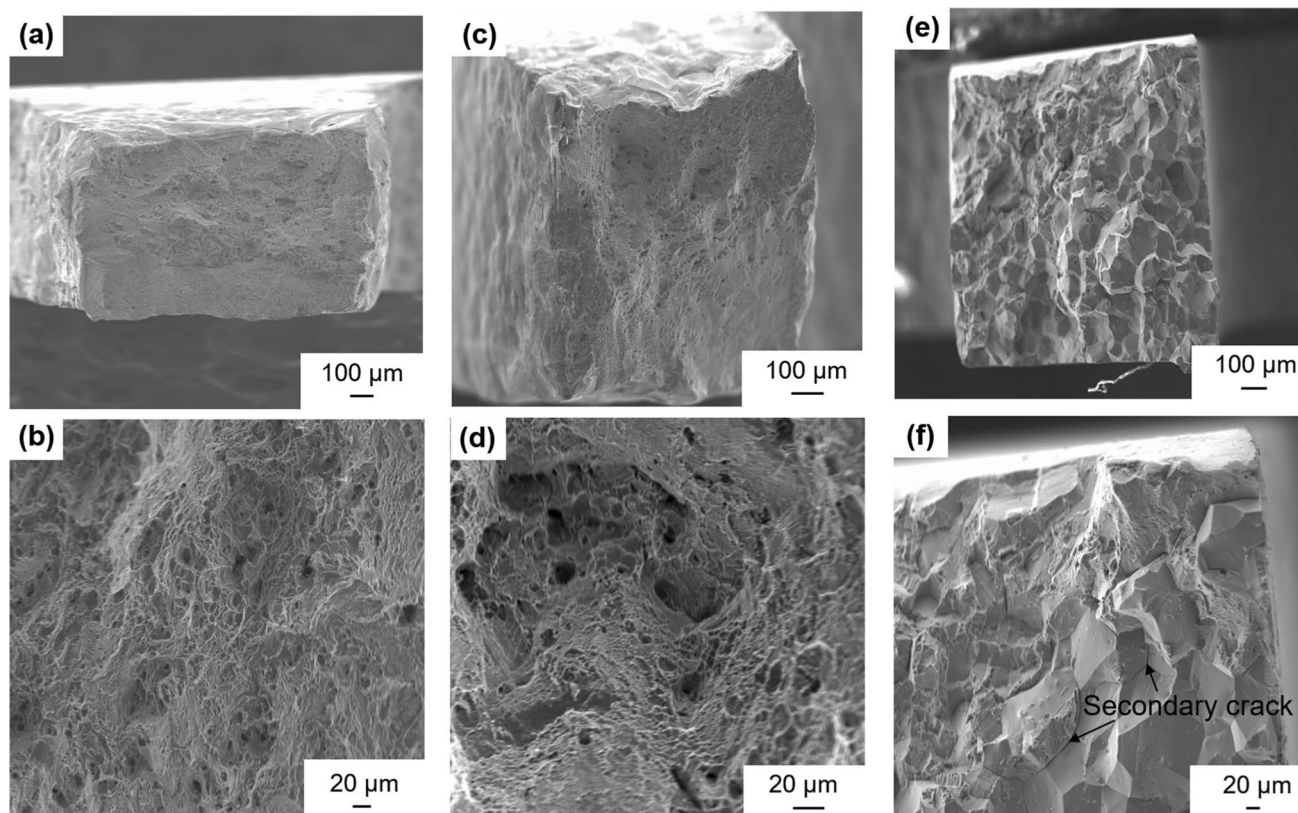


Fig. 12 SEM micrographs of the fracture surface of the BM tensioned at different temperatures: **a** and **b** RT, **c** and **d** 400 °C, **e** and **f** 700 °C

1. FSP was successfully applied to the high-strength and high-melting-point HT700 alloy with negligible wear of the tool. The microstructure with 4–6 μm equiaxed grains was obtained in the SZ.
2. Reducing the heat input is beneficial to improve the strength of FSP samples, so the optimal processing parameters in this work were rotation rate of 400 rpm and traverse speed of 50 mm/min.
3. Due to the reprecipitation of γ' phase of FSP samples tensioned at 700 °C, the yield strength of them increased clearly.
4. The microstructures of DCs, DWs, and DTZs were observed in the SZ as well as the HAGBs% of FSP samples was 58.1–65.1%, indicating that the grain refinement mechanism of HT700 alloy during FSP is CDRX.

Although the YS of FSP samples was not significantly enhanced, post-process heat treatment can improve the mechanical properties of FSP samples, which needs further investigation.

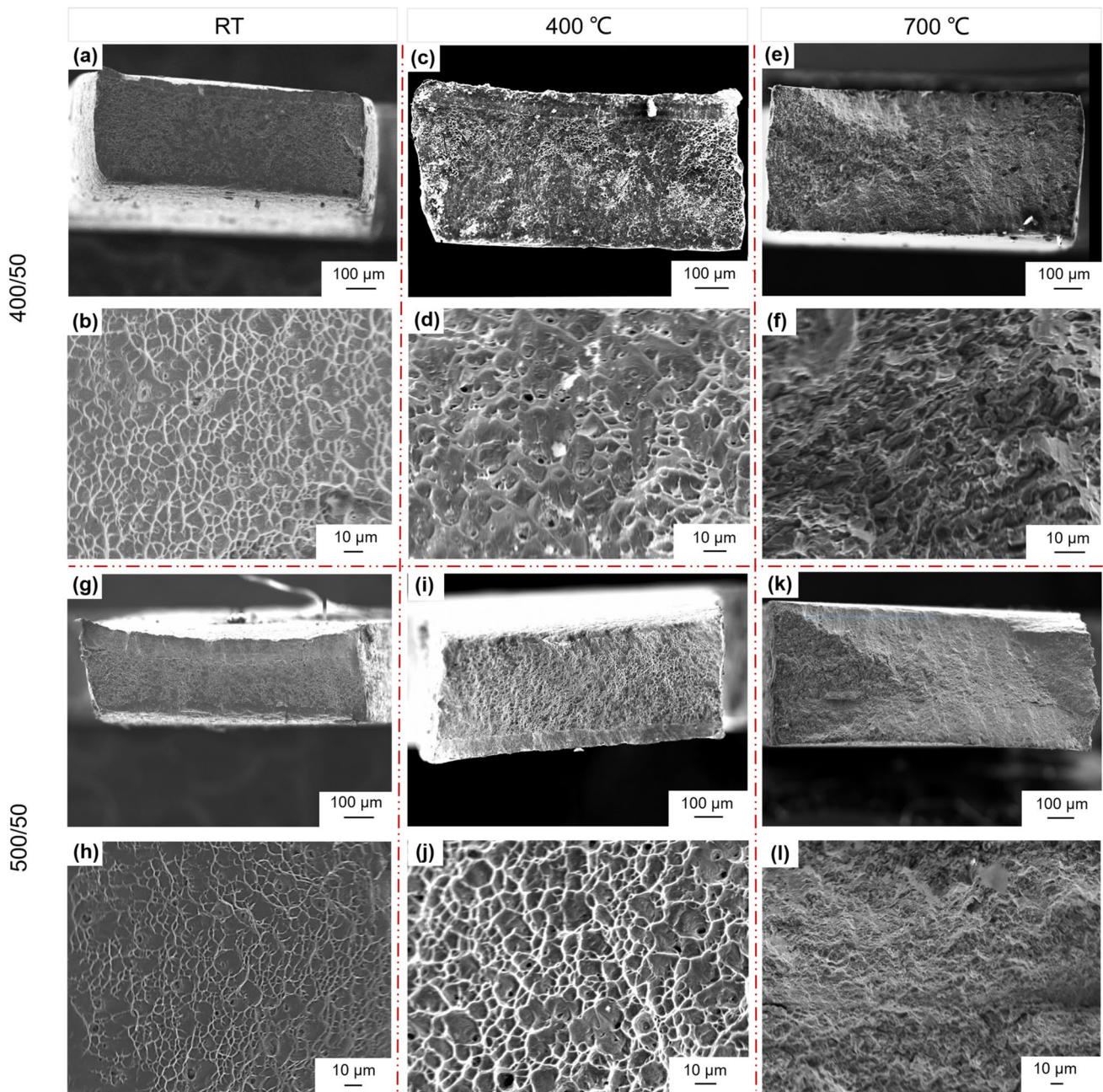


Fig. 13 SEM micrographs of the fracture surface of 400/50 and 500/50 tensioned at different temperatures

Acknowledgements We thank Zhiwei Wang, Cunlei Jia, Ning Li, Yandong Wang, Chunchun Yang, and Yaru Wang for technical assistance with the friction stir processing and helpful discussion. This work was supported by the National Natural Science Foundation of China (Grant Nos. 11872354 and 11627803), the National Key R&D Program of China (Nos. 2019YFA0705304 and 2017YFA0700703), and the Strategic Priority Research Program of the Chinese Academy of Sciences (Grant No. XDB22040502).

References

- [1] G.M. Liu, H.C. Yang, Q. Liang, X.C. Yang, S.P. Ren, J.H. Huang, *Acta Metall. Sin. (Engl. Lett.)* **30**, 863 (2017)
- [2] R. Viswanathan, K. Coleman, U. Rao, *Int. J. Pressure Vessels Pip.* **83**, 778 (2006)
- [3] Z. Zhong, Y. Gu, Y. Yuan, *Mater. Sci. Eng. A* **622**, 101 (2015)
- [4] M.A. Garakani, M. Mehdizadeh, *Mater. Des.* **32**, 2695 (2011)
- [5] H.U. Hong, I.S. Kim, B.G. Choi, M.Y. Kim, C.Y. Jo, *Mater. Sci. Eng. A* **517**, 125 (2009)
- [6] N.D. Evans, P.J. Maziasz, R.W. Swindeman, G.D. Smith, *Scr. Mater.* **51**, 503 (2004)

- [7] T.T. Wang, C.S. Wang, J.T. Guo, L.Z. Zhou, *Mater. Sci. Forum* **747–748**, 647 (2013)
- [8] Y. Yuan, Z.H. Zhong, Z.S. Yu, H.F. Yin, Y.Y. Dang, X.B. Zhao, Z. Yang, J.T. Lu, J.B. Yan, Y. Gu, *Mater. Sci. Eng. A* **619**, 364 (2014)
- [9] F. Sun, Y.F. Gu, J.B. Yan, Z.H. Zhong, M. Yuyama, *Acta Mater.* **102**, 70 (2016)
- [10] P. Xue, B.L. Xiao, Z.Y. Ma, *Scr. Mater.* **68**, 751 (2013)
- [11] Z.Y. Ma, *Metall. Mater. Trans. A* **39**, 642 (2008)
- [12] S. Mironov, Y.S. Sato, H. Kokawa, *Acta Mater.* **56**, 2602 (2008)
- [13] S. Mironov, Y.S. Sato, H. Kokawa, *Acta Mater.* **57**, 4519 (2009)
- [14] D.M. Sekban, S.M. Aktarer, H. Zhang, P. Xue, Z. Ma, G. Purcek, *Metall. Mater. Trans. A* **48**, 3869 (2017)
- [15] L. Wang, L. Xie, Y. Lv, L.C. Zhang, L. Chen, Q. Meng, J. Qu, D. Zhang, W. Lu, *Acta Mater.* **131**, 499 (2017)
- [16] N. Li, C.L. Jia, Z.W. Wang, L.H. Wu, D.R. Ni, Z.K. Li, H.M. Fu, P. Xue, B.L. Xiao, Z.Y. Ma, Y. Shao, Y.L. Chang, *Acta Metall. Sin. (Engl. Lett.)* **33**, 947 (2020)
- [17] H. Zhang, P. Xue, D. Wang, L.H. Wu, D.R. Ni, B.L. Xiao, Z.Y. Ma, *J. Mater. Sci. Technol.* **35**, 1278 (2019)
- [18] K.H. Song, H. Fujii, K. Nakata, *Mater. Des.* **30**, 3972 (2009)
- [19] F. Ye, H. Fujii, T. Tsumura, K. Nakata, *J. Mater. Sci.* **41**, 5376 (2006)
- [20] S.M. Mousavizade, M. Pouranvari, F. Malek Ghaini, H. Fujii, Y.F. Sun, *J. Alloys. Compd.* **685**, 806 (2016)
- [21] J.Y. Kim, W.S. Jung, W.S. Lee, J.W. Byeon, *Met. Mater. Int.* **22**, 694 (2016)
- [22] H.J. Liu, J.C. Hou, H. Guo, *Mater. Des.* **50**, 872 (2013)
- [23] M.M.Z. Ahmed, B.P. Wynne, J.P. Martin, *Sci. Technol. Weld. Join.* **18**, 680 (2013)
- [24] S. Guan, C.Y. Cui, *Acta Metall. Sin. (Engl. Lett.)* **28**, 1083 (2015)
- [25] W. Wang, P. Han, J. Yuan, P. Peng, Q. Liu, F. Qiang, K. Qiao, K.S. Wang, *Acta Metall. Sin. (Engl. Lett.)* **33**, 147 (2019)
- [26] Y. Ni, D.Q. Qin, Y. Mao, X. Xiao, *Int. J. Adv. Manuf. Technol.* **106**, 3273 (2020)
- [27] M. Ghosh, K. Kumar, R.S. Mishra, *Mater. Sci. Eng. A* **528**, 8111 (2011)
- [28] E. Gharibshahiyan, A.H. Raouf, N. Parvin, *IARJSET* **2**, 11 (2015)
- [29] B. Du, Z. Hu, J. Wang, L. Sheng, H. Zhao, Y. Zheng, T. Xi, *Bioact. Mater.* **5**, 219 (2020)
- [30] Z.W. Wang, G.M. Xie, D. Wang, H. Zhang, D.R. Ni, P. Xue, B.L. Xiao, Z.Y. Ma, *Acta Metall. Sin. (Engl. Lett.)* **33**, 58 (2019)
- [31] L.H. Wu, D. Wang, B.L. Xiao, Z.Y. Ma, *Scr. Mater.* **78–79**, 17 (2014)
- [32] W. Wang, P. Han, P. Peng, T. Zhang, Q. Liu, S.N. Yuan, L.Y. Huang, H.L. Yu, K. Qiao, K.S. Wang, *Acta Metall. Sin. (Engl. Lett.)* **33**, 43 (2019)
- [33] P.B. Prangnell, C.P. Heason, *Acta Mater.* **53**, 3179 (2005)
- [34] D.P. Field, T.W. Nelson, Y. Hovansk, K.V. Jata, *Metall. Mater. Trans. A* **32**, 2869 (2001)
- [35] G.R. Cui, Z.Y. Ma, S.X. Li, *Acta Mater.* **57**, 5718 (2009)
- [36] H. Zhao, Q. Pan, Q. Qin, Y. Wu, X. Su, *Mater. Sci. Eng. A* **751**, 70 (2019)
- [37] X.C. Luo, L.M. Kang, H.L. Liu, Z.J. Li, Y.F. Liu, D.T. Zhang, D.L. Chen, *Mater. Sci. Eng. A* **797**, 139945 (2020)
- [38] Y.S. Sato, M. Urata, H. Kokawa, *Metall. Mater. Trans. A* **33**, 625 (2002)
- [39] X.C. Liu, Y.F. Sun, T. Nagira, H. Fujii, *Mater. Charact.* **137**, 24 (2018)
- [40] B.N. Du, Z.Y. Hu, L.Y. Sheng, D.K. Xu, Y.X. Qiao, B.J. Wang, J. Wang, Y.F. Zheng, T.F. Xi, *J. Mater. Sci. Technol.* **60**, 44 (2021)
- [41] H. Jazaeri, F.J. Humphreys, *Acta Mater.* **52**, 3239 (2004)
- [42] H. Jazaeri, F.J. Humphreys, *Acta Mater.* **52**, 3251 (2004)
- [43] H. Jazaeri, F.J. Humphreys, *J. Microsc.* **213**, 241 (2004)
- [44] Y.J. Chen, Y.J. Li, J.C. Walmsley, S. Dumoulin, H.J. Roven, *Metall. Mater. Trans. A* **41**, 787 (2009)
- [45] Y. Liu, Y. Cai, C. Tian, G. Zhang, G. Han, S. Fu, C. Cui, Q. Zhang, *J. Mater. Sci. Technol.* **49**, 35 (2020)
- [46] S. Fu, T. Cheng, Q. Zhang, Q. Hu, P. Cao, *Acta Mater.* **60**, 6650 (2012)
- [47] H. Jiang, Q. Zhang, X. Chen, Z. Chen, Z. Jiang, X. Wu, J. Fan, *Acta Mater.* **55**, 2219 (2007)
- [48] G.M. Han, C.G. Tian, C.Y. Cui, Z.Q. Hu, X.F. Sun, *Acta Metall. Sin. (Engl. Lett.)* **28**, 542 (2015)
- [49] W. Mangen, E. Nembach, *Acta Metall.* **37**, 1451 (1989)
- [50] R.W. Kozar, A. Suzuki, W.W. Milligan, J.J. Schirra, M.F. Savage, T.M. Pollock, *Metall. Mater. Trans. A* **40**, 1588 (2009)
- [51] C.Y. Cui, Y.F. Gu, Y. Yuan, T. Osada, H. Harada, *Mater. Sci. Eng. A* **528**, 5465 (2011)
- [52] B. Du, Z. Hu, L. Sheng, C. Cui, J. Yang, Y. Zheng, X. Sun, *J. Mater. Sci. Technol.* **34**, 1805 (2018)
- [53] Y. Xu, W. Li, X. Yang, Y. Gu, *Mater. Sci. Eng. A* **788**, 139596 (2020)
- [54] P. Liu, R. Zhang, Y. Yuan, C. Cui, F. Liang, X. Liu, Y. Gu, Y. Zhou, X. Sun, *J. Mater. Sci. Technol.* **77**, 66 (2021)
- [55] K.H. Song, K. Nakata, *Mater. Des.* **31**, 2942 (2010)
- [56] J. Rodelas, J. Lippold, *Metallogr. Microstruct. Anal.* **2**, 1 (2013)
- [57] L.Y. Sheng, B.N. Du, Z.Y. Hu, Y.X. Qiao, Z.P. Xiao, B.J. Wang, D.K. Xu, Y.F. Zheng, T.F. Xi, *J. Magnes. Alloy* **8**, 601 (2020)
- [58] Z. Zhong, Y. Gu, T. Osada, Y. Yuan, C. Cui, T. Yokokawa, T. Tetsui, H. Harada, *J. Mater. Sci.* **46**, 7573 (2011)